Gastroenterology 2016;151:1176–1191

BASIC AND TRANSLATIONAL—LIVER

Combination of Mass Cytometry and Imaging Analysis Reveals Origin, Location, and Functional Repopulation of Liver Myeloid Cells in Mice

Bruna Araujo David,[1] Rafael Machado Rezende,[2] Maísa Mota Antunes,[1] Mônica Morais Santos,[1] Maria Alice Freitas Lopes,[1] Ariane Barros Diniz,[1] Rafaela Vaz Sousa Pereira,[1] Sarah Cozzer Marchesi,[1] Débora Moreira Alvarenga,[1] Brenda Naemi Nakagaki,[1] Alan Moreira Araújo,[1] Daniela Silva dos Reis,[3] Renata Monti Rocha,[3] Pedro Elias Marques,[3] Woo-Yong Lee,[4] Justin Deniset,[4] Pei Xiong Liew,[4] Stephen Rubino,[2] Laura Cox,[2] Vanessa Pinho,[5] Thiago Mattar Cunha,[6] Gabriel Rocha Fernandes,[7] André Gustavo Oliveira,[1,8] Mauro Martins Teixeira,[3] Paul Kubes,[4] and Gustavo Batista Menezes[1]

[1]Center for Gastrointestinal Biology, Departamento de Morfologia, Instituto de Ciências Biológicas, Universidade Federal de Minas Gerais, Belo Horizonte, Minas Gerais, Brazil; [2]Ann Romney Center for Neurologic Diseases, Brigham and Women's Hospital, Harvard Medical School, Boston, Massachusetts; [3]Departamento de Bioquímica e Imunologia, Instituto de Ciências Biológicas, Universidade Federal de Minas Gerais, Belo Horizonte, Minas Gerais, Brazil; [4]University of Calgary, Alberta, Canada; [5]Resolution of Inflammation Lab, Departamento de Morfologia, Instituto de Ciências Biológicas, Universidade Federal de Minas Gerais, Belo Horizonte, Minas Gerais, Brazil; [6]Faculdade de Medicina de Ribeirão Preto, Universidade de São Paulo, São Paulo, Brazil; [7]Centro de Pesquisas René Rachou, FIOCRUZ, Belo Horizonte, Minas Gerais, Brazil; and [8]Departamento de Fisiologia, Instituto de Ciências Biológicas, Universidade Federal de Minas Gerais, Belo Horizonte, Minas Gerais, Brazil

See editorial on page 1065.

BACKGROUND & AIMS: Resident macrophages are derived from yolk sac precursors and seed the liver during embryogenesis. Native cells may be replaced by bone marrow precursors during extensive injuries, irradiation, and infections. We investigated the liver populations of myeloid immune cells and their location, as well as the dynamics of phagocyte repopulation after full depletion. The effects on liver function due to the substitution of original phagocytes by bone marrow–derived surrogates were also examined. **METHODS:** We collected and analyzed liver tissues from C57BL/6 (control), *LysM-EGFP, B6 ACTb-EGFP, CCR2*$^{-/-}$, *CD11c-EYFP, CD11c-EYFP-DTR,* germ-free mice, *CX3CR1*$^{gfp/gfp}$, *CX3CR1*$^{gpf/wt}$, and *CX3CR1-DTR-EYFP*. Liver nonparenchymal cells were immunophenotyped using mass cytometry and gene expression analyses. Kupffer and dendritic cells were depleted from mice by administration of clodronate, and their location and phenotype were examined using intravital microscopy and time-of-flight mass cytometry. Mice were given acetaminophen gavage or intravenous injections of fluorescently labeled *Escherichia coli*, blood samples were collected and analyzed, and liver function was evaluated. We assessed cytokine profiles of liver tissues using a multiplexed array. **RESULTS:** Using mass cytometry and gene expression analyses, we identified 2 populations of hepatic macrophages and 2 populations of monocytes. We also identified 4 populations of dendritic cells and 1 population of basophils. After selective depletion of liver phagocytes, intravascular myeloid precursors began to differentiate into macrophages and dendritic cells; dendritic cells migrated out of sinusoids, after a delay, via the chemokine CX3CL1. The cell distribution returned to normal in 2 weeks, but the repopulated livers were unable to fully respond to drug-induced injury or clear bacteria for at least 1 month. This defect was associated with increased levels of inflammatory cytokines, and dexamethasone accelerated the repopulation of liver phagocytes. **CONCLUSIONS:** In studies of hepatic phagocyte depletion in mice, we found that myeloid precursors can differentiate into liver macrophages and dendritic cells, which each localize to distinct tissue compartments. During replenishment, macrophages acquire the ability to respond appropriately to hepatic injury and to remove bacteria from the blood stream.

Keywords: CyTOF; DC; Liver Development; Mouse Model.

The liver is a key organ for immune maturation during embryogenesis[1,2] and also plays an essential role in immune surveillance throughout life. The hepatic environment physiologically harbors a vast population of immune cells, including natural killer (NK)[3] and NK T cells,[4] dendritic cells (DCs),[5] and macrophages (Kupffer cells [KCs]).[6] In order to accomplish critical innate immune functions, phagocytic cells are strategically positioned within hepatic compartments. KCs are located in the

Abbreviations used in this paper: **APAP, acetaminophen; BM, bone marrow; CLL, clodronate-loaded liposomes; CyTOF, time-of-flight mass cytometry; DC, dendritic cell; GFP, green fluorescent protein; HSC, hepatic stellate cell; ICG, indocyanine green; IL, interleukin; KC, Kupffer cell; NK, natural killer cell.**

Most current article

0016-5085/$36.00
http://dx.doi.org/10.1053/j.gastro.2016.08.024

sinusoidal lumen, where they are constantly surveying blood content, ingesting aging erythrocytes,[7,8] and catching pathogens out of the mainstream of blood.[9,10]

Recent studies have shown that macrophages seed the liver during embryogenesis from yolk sac progenitors, and this resident pool may be maintained in adulthood via both self-renewal of precursors and, to a lesser extent, recruitment of bone marrow (BM)–derived cells. Indeed, there is a growing body of evidence that the KC population is composed mainly of cells related to embryonic precursors rather than hematopoietic cells.[11,12] DCs develop from BM-derived hematopoietic stem cells, but circulating monocyte precursors can also contribute to the resident DC pool.[13] A small population of liver DCs have been described previously[14–16]; however, in vivo studies aiming to define the precise location and actual density of DCs within the liver, as well as their relationship with other hepatic cells are needed. Additionally, despite being described as phagocytes, their ability to engulf and destroy whole pathogens remains debatable.[17]

The resident DC and KC liver populations in adulthood, therefore, are some combination of embryonic-derived precursors and monocyte-derived cells, and it is likely that multiple factors define the extent of the contribution of these 2 sources.[2] However, during *emergency repopulation*—a term we coined for the sudden complete loss of immune cells due to toxins, pathogens (ie, *Listeria*), or trauma—self-replication may not be an option. Here we used a combination of high-throughput analysis with live-imaging approaches to precisely determine phagocytic populations within the liver and the functional consequences of their replenishment by BM cells.

Methods

Experimental Procedures

Animals. C57BL/6 wild type, LysM-EGFP ($Lyz2^{tm1.1Graf}$), B6 ACTb-EGFP ($C57BL/6^{Tg(CAG-EGFP)1Osb/J}$; chicken beta actin), CCR2$^{-/-}$ (B6.129S4-$Ccr2^{tm1Ifc}$/Jand), CD11c-EYFP ($NOD.^{Cg-Tg(Itgax-Venus)1Mnz/QtngJ}$) mice were from Centro de Bioterismo in Universidade Federal de Minas Gerais (CEBIO–UFMG, Brazil). Germ-free Swiss/NIH mice were derived from a germ-free nucleus (Taconic Farms, Hudson, NY). CD11c-EYFP-DTR, CX3CR1$^{gfp/gfp}$ and CX3CR1$^{gpf/wt}$ ($B6.129P-^{Cx3cr1tm1Litt/J}$) were from Animal Facility of University of Calgary (Alberta, Canada). CX3CR1-DTR-EYFP ($B6.129P2^{(Cg)-Cx3cr1tm2.1(cre/ERT2)Litt/WganJ}$) mice were from Animal Facility of Harvard Institutes of Medicine (Boston, MA). Mice that expressed diphtheria toxin receptor received tamoxifen (10 mg/mouse in peanut oil, intraperitoneally) for 5 consecutive days and were treated with diphtheria toxin (500 ng/mouse, in sterile phosphate-buffered saline; intraperitoneally) for 2 consecutive days for selective depletion before experiments. CD11c-DTR mice were treated with diphtheria toxin at the same regimen from CX3CR1-DTR. All animals were housed in a conventional specific pathogen-free facility at the Universidade Federal de Minas Gerais, Harvard Institutes of Medicine and University of Calgary, according to the animal protocol, with the full knowledge and permission of the Standing Committee on Animals at all institutions.

Confocal Microscopy and Immunohistochemistry

Confocal intravital imaging was performed as described previously.[18] Before surgery, mice received a single dose or a mixture of the following antibodies or fluorescent probes: anti-F4/80 phycoerythrin (4 μg, clone BM8, eBiosciences, San Diego, CA), anti-CD31 BV-421 (4 μg, clone MEC 13.3, BD Horizon, San Jose, CA), anti-CX3CL1 phycoerythrin (60 μL per mouse; eBiosciences), 4′,6-diamidino-2-phenylindole (0.1 mL at 1 mM; Sigma, St Louis, MO), and albumin fluorescein isothiocyanate (0.1 mL at 5 mg per mL). Liver fragments were also stained with anti-podoplanin phycoerythrin (1:50 solution; BioLegend, San Diego, CA), anti–green fluorescent protein (GFP) (1:50 solution; Santa Cruz Biotechnology, Santa Cruz, CA), or desmin (1:50; Dako, Carpinteria, CA) for ex vivo images. Alexa Fluor 586–conjugated goat anti-mouse was used as secondary antibody for desmin experiments (1:50, Thermo Fisher Scientific, Logan, UT). Vitamin A autofluorescence was imaged using a 405-nm laser. Mice were imaged using Nikon Eclipse Ti with a C2 confocal. Cell density, location, and 3-dimensional rendering were made using Volocity (6.3) (Perkin Elmer, Waltham, MA).

Liver Nonparenchymal Cells

Liver nonparenchymal cells were isolated as reported previously.[19] Livers were digested in a collagenase solution and cells were differentially separated by centrifugation. For time-of-flight mass cytometry (CyTOF) experiments, 1×10^6 cells were stained with isotope-conjugated antibodies as described.[20] Events were gated for CD45$^+$ cells, and T cells, B cells, red blood cells, and hepatic stellate cells (HSCs) were excluded from analysis. NK cells frequency was investigated by fluorescence-activated cell sorting (CD11c$^+$CD3$^-$NKp46$^+$NK1.1$^+$). Absence of HSCs in these samples was also checked by reverse transcription polymerase chain reaction. A complete list of antibody panels and genes used in reverse transcription polymerase chain reaction (Taqman probes) can be found in Supplementary Table 1. Samples were acquired with a Helios Mass Cytometer (Fluidigm, South San Francisco, CA) and data were plotted using viSNE analysis as described previously. Gates were done as described in Results section.

For Nanostring experiments, liver nonparenchymal cells were isolated from CX3CR1$^{gfp/wt}$ mice and stained with anti-F4/80 allophycocyanin (1:100, clone BM8; eBiosciences). Samples were acquired using cell sorter FACSAria III and gates were made in F4/80$^+$CX3CR1$^-$ for intravascular cells and F4/80$^-$CX3CR1$^+$ for extravascular cells. Splenic DCs were sorted as CD11c$^+$ F4/80$^-$ cells and peritoneal macrophages were collected by lavage and sorted as F4/80$^+$ cells. Approximately 1×10^5 of each cell type was sorted, and each sample consisted in a pool of 2 mice, and 3 samples were run independently.

Bone Marrow Isolation

BM cells were harvested from mouse femurs and tibia using a needle to remove the cells from the medullary cavity.[21] BM chimeras were performed as described previously.[22] In these experiments, wild-type mice received 10^7 BM cells intravenously from B6 ACTb-EGFP mice and were allowed to recover for 6 weeks before experiments.

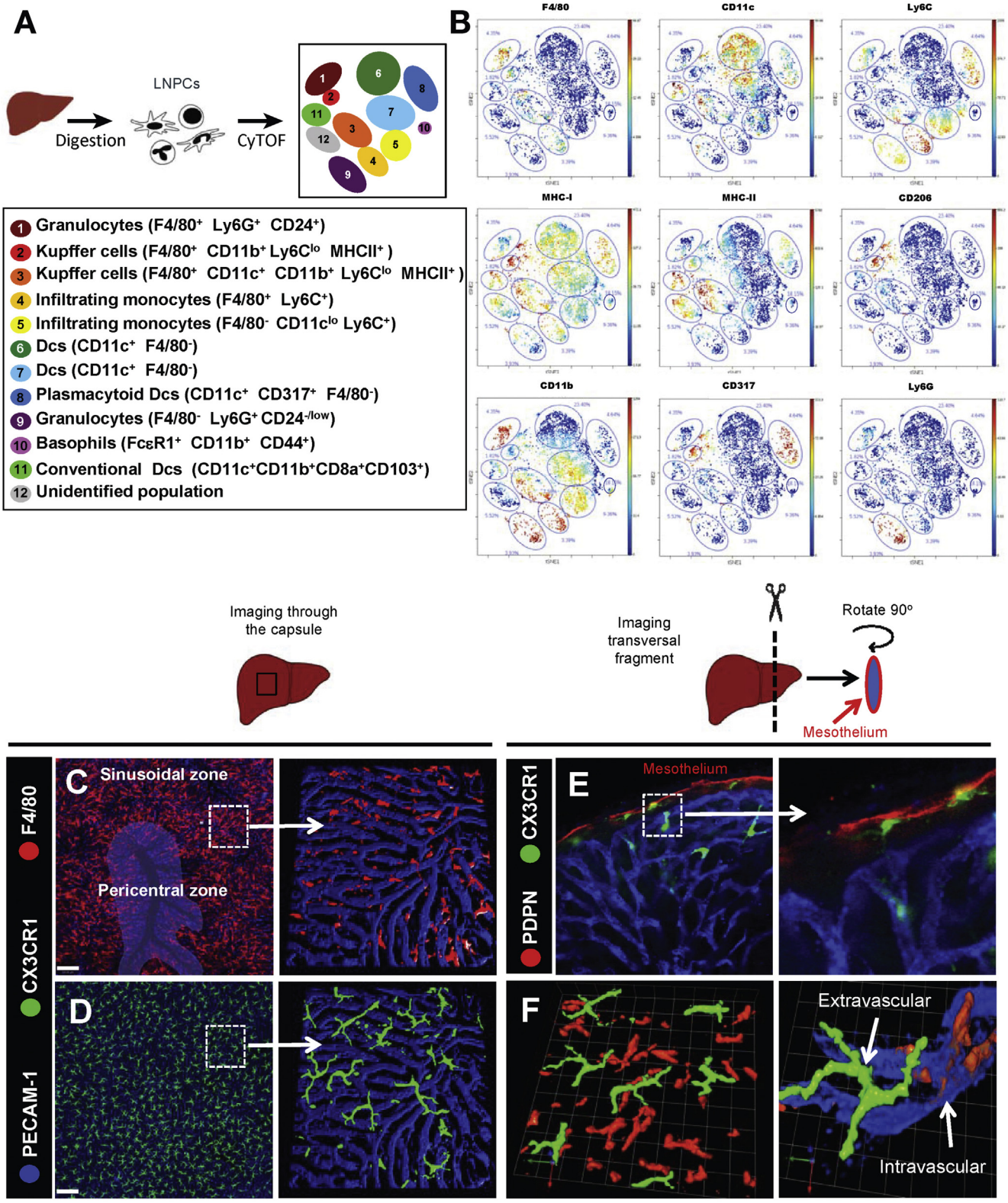

Figure 1. Identification of liver phagocytes by CyTOF and intravital microscopy. (*A*) Schematic representation of isolation liver nonparenchymal cells (LNPC) and clustering after CyTOF analysis. (*B*) *Dot plot* representation of viSNE analysis showing different clusters and the expression of several different surface markers that enable the distinction of immune populations. (*C*) Liver confocal intravital microscopy imaging through the capsule evidencing the distribution of F4/80$^+$ cells (Kupffer cells; in *red*; anti-F4/80) in different liver regions. (*D*) Same as (*C*) but for CX3CR1$^+$ cells (CX3CR1$^{gfp/wt}$ mice). (*E*) Ex vivo imaging of liver fragment revealed that DCs (CX3CR1$^+$ cells) are mainly located under the mesothelium (stained with anti-podoplanin). (*F*) Three-dimensional rendering of F4/80$^+$ (intravascular) and CX3CR1$^+$ cells (extravascular) showing their different spatial location. *Scale bars* = 120 μm. Error bars indicate the mean ± SEM. *$P < .05$ (unpaired *t* test). n = 5/group.

Drug-Induced Liver Injury Model and Clodronate-Induced Depletion

Acetaminophen (APAP; 600 mg per kg; Sigma) was dissolved in warm saline before gavage and serum alanine aminotransferase was estimated as described.[21] Indocyanine green (ICG; Sigma) clearance by the liver was estimated in serum after injecting a single dose of 20 mg per kg intravenously. Blood was collected 20 minutes after injection and the amount of ICG was determined by spectrophotometry (absorbance in 800 nm). KC/DC depletion was achieved by intravenous injection of 200 μL clodronate liposomes (ClodronateLiposomes.com) 48 hours before experiments. In dexamethasone treatment protocol, mice received a daily intraperitoneal dose of 5 mg/kg of dexa dissolved in corn oil during 7 days.

Systemic Escherichia coli *Injection*

Escherichia coli GFP (ATCC 25922GFP) were cultivated in Luria broth medium (MP Biomedicals, Santa Ana, CA). In flow cytometry experiments, mice intravenously received 10^6 *E coli* and blood was collected after 5 minutes. Blood samples were immediately diluted in phosphate-buffered saline (1:20) and read in cytometer. To in vivo imaging of *E coli* capture, mice received 10^7 *E coli* intravenously and were imaged under confocal microscopy for 5 minutes.

Multiplex Cytokine Array

Liver samples were weighted (50 mg) and homogenized. Cytokine concentration in the supernatant was dosed following manufacture's instruction (Milliplex MCYTOMAG- 0K-32. Mouse Cytokine MAGNETIC Kit).

Expression Data Analysis

Expression abundance was obtained by Nanostring nCounter mouse Immunology Assay. The correlation of gene expression among different cell types were calculated and plotted as heatmap using the R platform. Differentially expressed genes were identified by DESeq2 R Package. Statistically relevant results are considered with $P < .05$ and a fold change of at least 50% higher or lower. Pathways and functional classification were done by cross association using Kyoto Encyclopedia of Genes and Genomes Pathways and Kyoto Encyclopedia of Genes and Genomes Brite databases.

Statistical Analyses

Experimental data analysis was performed with one-way analysis of variance (one-way analysis of variance with Tukey's post-hoc test) and unpaired Student *t* test provided by Prism 5.0 software (GraphPad, La Jolla, CA). All data are given as the mean ± SEM. In vivo experimental groups had at least 5 mice per group. Data shown are representative of at least 2 independent experiments. Differences were considered to be significant at $P < .05$.

Results

High-Dimensional Identification of Liver Phagocytes

To better characterize the resident phagocytic populations, we purified liver nonparenchymal cells ($CD45^+$ liver nonparenchymal cells) and performed CyTOF analysis, which allows for simultaneous staining with multiple combinations of cell markers, and can reveal new immune cell populations that would not be uncovered by conventional flow cytometry. In these experiments, we gated on $CD45^+$ cells and excluded red blood cells, Ito cells, and B and T cells during analysis. Using an unbiased viSNE analysis to map high-dimensional cytometry data, we identified 12 clusters of liver nonparenchymal cells (Figure 1*A*). The majority of cells mapped to either F4/80 (clusters 1–4) or CD11c (clusters 5–8) (Figure 1*A* and *B*). Cluster 1 was defined as mature granulocytes due to intermediate expression level of Ly6G (Figure 1*A* and *B*) and high expression of CD24 (Supplementary Figure 1*A*). Based on the expression of F4/80, MHC-II, and CD11b (Figure 1*A* and *B*), we defined 2 different populations of KCs (clusters 2 and 3). KC cluster 2 expressed CD206, CD317, and CD1d, whereas cluster 3 was negative for CD206, CD317, and CD1d, but expressed CD11c (Figure 1*A* and Supplementary Figure 1*A*). Cluster 4 and 5 were characterized as infiltrating monocytes because they were $CD11b^+Ly6C^+MHC\text{-}I^{int}MHC\text{-}II^{lo}$, but cluster 5 was $F4/80^-$ and $CD11c^{lo}$ (Figure 1*A* and *B*). Clusters 6–8 and 11 were categorized as DCs, because they were $CD11c^+CD11b^{int/hi}F4/80^-Ly6G^-MHC\text{-}I^+MHC\text{-}II^{+/lo}$. Cluster 8 was defined as plasmacytoid DCs due to their high expression of the plasmacytoid DC marker CD317 (Figure 1*A* and *B*). Cluster 9 was also defined as granulocytes according to their high expression of Ly6G, CD11b, and Gr1, as well as intermediate expression of CD24 and Ly6C (Figure 1*A* and *B* and Supplementary Figure 1*A*). Finally, cells that expressed the high-affinity IgE receptor (FcεRI), together with CD44 and CD11b, were clustered as basophils (cluster 10) (Figure 1*A* and *B* and Supplementary Figure 1*A*). Cluster 11 may represent a population of conventional DCs due to the expression of CD11c, CD11b, CD8a, and CD103 (Figure 1*A* and *B* and Supplementary Figure 1*A*). $CD11c^+$ NK cells (NK1.1 and NKp46) comprised an insignificant population in this setup (<0.2%) and were not considered during analysis (Supplementary Figure 1*B*). Cluster 12 could not be categorized using the markers chosen for this experiment. A schematic clustering explanation is depicted in Figure 1*A*.

To spatially resolve the location and the relationship between the main $F4/80^+$ and $CD11c^+$ populations, we imaged the liver by confocal intravital microscopy.[18] We first identified the main vascular arrangements that could constitute points of reference for the location of different liver immune cells (Supplementary Figure 2 and Supplementary Movie 1). Based on in vivo blood flow tracking, 2 main vascular regions were defined: the area surrounding a centrilobular vein was termed the *pericentral zone*, and the remaining areas in between were referred to as the sinusoidal zone (Figure 1*C*). In an expanded field of view, we observed that $F4/80^+$ cells were not homogeneously distributed within the liver, as they accumulated preferentially in the sinusoidal zone rather than in pericentral areas (Figure 1*C*). Three-dimensional reconstruction showed that these cells inhabited the intravascular compartment exclusively and specifically (Figure 1*C* and

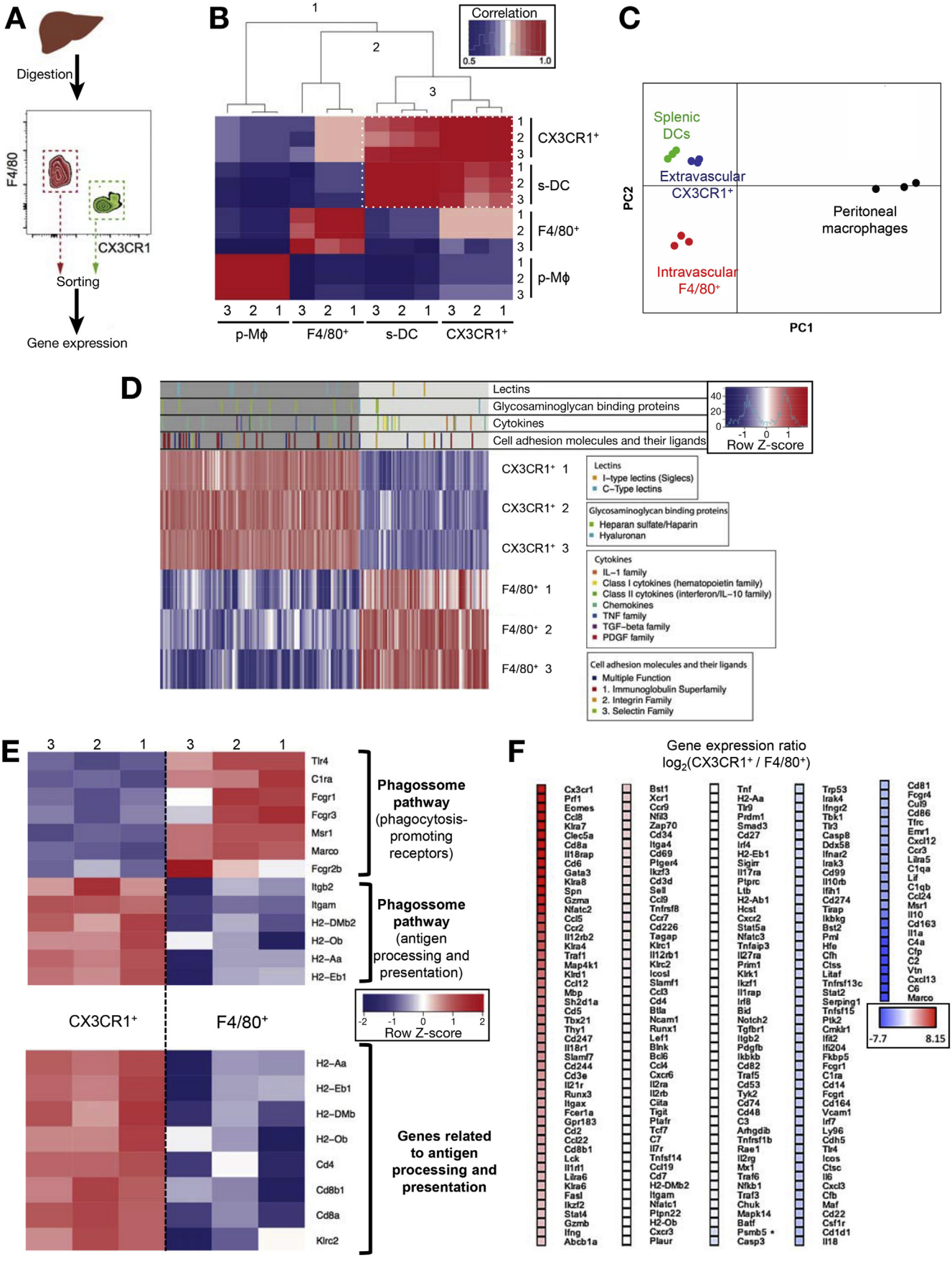
A
Digestion
F4/80
CX3CR1
Sorting
Gene expression
B
Correlation
0.5
1.0
CX3CR1+
s-DC
F4/80+
p-Mϕ
C
Splenic DCs
Extravascular CX3CR1+
Peritoneal macrophages
Intravascular F4/80+
PC2
PC1
D
Lectins
Glycosaminoglycan binding proteins
Cytokines
Cell adhesion molecules and their ligands
Row Z-score
CX3CR1+ 1
CX3CR1+ 2
CX3CR1+ 3
F4/80+ 1
F4/80+ 2
F4/80+ 3
Lectins
I-type lectins (Siglecs)
C-Type lectins
Glycosaminoglycan binding proteins
Heparan sulfate/Haparin
Hyaluronan
Cytokines
IL-1 family
Class I cytokines (hematopoietin family)
Class II cytokines (interferon/IL-10 family)
Chemokines
TNF family
TGF-beta family
PDGF family
Cell adhesion molecules and their ligands
Multiple Function
1. Immunoglobulin Superfamily
2. Integrin Family
3. Selectin Family
E
Tlr4
C1ra
Fcgr1
Fcgr3
Msr1
Marco
Fcgr2b
Itgb2
Itgam
H2-DMb2
H2-Ob
H2-Aa
H2-Eb1
Phagossome pathway (phagocytosis-promoting receptors)
Phagossome pathway (antigen processing and presentation)
Row Z-score
CX3CR1+
F4/80+
H2-Aa
H2-Eb1
H2-DMb
H2-Ob
Cd4
Cd8b1
Cd8a
Klrc2
Genes related to antigen processing and presentation
F
Gene expression ratio
log2(CX3CR1+ / F4/80+)
-7.7
8.15

Supplementary Movie 2). Consistent with this, all F4/80$^+$ cells were also positive for lysozyme M, a marker for macrophages (LysM-EGFP mice; Supplementary Figure 3*A*), confirming that all of these cells were KCs and none were ever seen in the parenchyma.

Intravital imaging also revealed a large hepatic population of CD11c$^+$ cells with differential spatial distribution (CD11c-EYFP reporter mice; Supplementary Figure 3*B*). The CD11c$^+$F4/80$^-$ population was larger in size, displayed numerous dendrites on their surface and inhabited the extravascular space, suggestive of a population of DCs (Supplementary Movie 3). However, as mentioned, CD11c$^+$F4/80$^+$ cells were also observed lining the intravascular area, and resembled KC morphology validating 2 different KC populations from CyTOF (Figure 1*B*, Supplementary Figure 3*B* and Supplementary Movie 3). CD11c expression in both intravascular and extravascular populations was confirmed by CD11c-targeted depletion (CD11c-DTR-EYFP mice), which caused full depletion of extravascular CD11c$^+$ cells and also a significant decrease (approximately 50%) in intravascular CD11c$^+$F4/80$^+$ cells (Supplementary Figure 3*C*).

To image just the extravascular cells, we used CX3CR1$^{gfp/wt}$ reporter mice because CX3CR1 is expressed on DCs,[23] but not on mature KCs under homeostatic conditions.[11] We found an exclusively extravascular population of CX3CR1$^+$ cells (Figure 1*D* and Supplementary Movie 4), which were similar in shape and number to an extravascular CD11c$^+$F4/80$^-$ population (Supplementary Figure 3*B*). Intravital images through the liver surface showed that CX3CR1$^+$ cells are abundant and uniformly distributed in the field of view; however, ex vivo imaging of liver fragments using transversal slices revealed that such spider-like CX3CR1$^+$ cells were found mainly under a thin layer of mesothelium that covers the liver (Figure 1*E*), and were not distributed throughout the sinusoids as KCs. Also, CX3CR1$^+$ cells were CD11c$^+$ (Supplementary Figure 4*A*), but negative for desmin (Supplementary Figure 5*A*), excluding them as a population of HSCs. Of note, CD11c$^+$ cells were also negative for desmin (Supplementary Figure 5*A*). Deeper imaging within the liver showed that some CX3CR1$^+$ cells were also found surrounding larger hepatic vessels (Supplementary Figure 4*B* and *C*). As seen in higher magnification of 3-dimensional reconstructions, there is intimate contact of some F4/80$^+$ intravascular and CX3CR1$^+$ extravascular cells, and the latter emit protrusions to reach the vessel lumen (Figure 1*F*). To confirm that extravascular, and not intravascular, cells specifically expressed CX3CR1, we used a mouse strain that has both DTR and EYFP expression under control of CX3CR1 (CX3CR1 [CreER]-DTR-EYFP). Treatment with diphtheria toxin led to 95% depletion of extravascular CX3CR1$^+$ cells, with no detectable effects on intravascular F4/80$^+$ cells, validating CX3CR1 as a selective marker for extravascular cells under homeostatic conditions (monitored by intravital microscopy; Supplementary Figure 3*D*).

Next, we isolated extravascular CX3CR1$^+$F4/80$^-$ and intravascular CX3CR1$^-$F4/80$^+$ cells by sorting (Figure 2*A*) and dissected their phenotypic identities by measuring gene expression using the Nanostring nCounter mouse immunology assay, a multiplexed messenger RNA hybridization approach. We excluded the presence of HSCs in these samples because, after our isolation procedure, we did not detect the expression of HSCs common genes (Supplementary Figure 5*B*). Also, we did not detect vitamin A granules by either intravital microscopy (Supplementary Figure 5*C*) or fluorescence-activated cell sorting (Supplementary Figure 5*D*). Both liver-isolated populations clustered together when compared with a liver-unrelated cell (activated peritoneal macrophage; Figure 2*B* and *C*). This approach suggests that the extravascular CX3CR1$^+$F4/80$^-$ and intravascular CX3CR1$^-$F4/80$^+$ cells have a similar source and/or environment dictating their clustered genotype.

However, functional category analysis showed that intra- and extravascular cells had a differential expression of genes belonging to C- and I-type lectins, glycosaminoglycan-binding proteins, cytokines, and various other molecules (Figure 2*C* and GEO accession number: GSE81645). Phagocytosis-promoting receptors were significantly enriched on the CX3CR1$^-$F4/80$^+$ population (Figure 2*E*), suggesting an active role in recognition and clearance of bacteria or antigens from the circulation. In line with this, CX3CR1$^-$F4/80$^+$ cells had significantly higher expression of macrophage-related genes, such as *Marco*, *Cd163*, and *Mrs1* (Figure 2*F*). By contrast, CX3CR1$^+$F4/80$^-$ cells had enriched pathways involved in antigen processing and presentation (Figure 2*E*), with higher expression of DC common genes, including *Cx3cr1*, *Prf1*, and *Itgax* (Figure 2*F*). In fact, hierarchical clustering (Figure 2*B*) and principal coordinate analysis (Figure 2*C*) confirmed that the genetic profile of CX3CR1$^+$F4/80$^-$ cells was closely related to a classic DC isolated from the spleen. Taking together the expression of surface markers, cell morphology, and genetic profile, we established that extravascular CX3CR1$^+$F4/80$^-$ cells are a population of liver DCs that are located mainly in the submesothelial space, while intravascular CX3CR1$^-$F4/80$^+$ cells comprised the hepatic resident macrophages, or KCs.

Figure 2. Genetic profiles of different liver phagocytes. (*A*) Schematic representation of isolation and sorting of CX3CR1$^+$ and F4/80$^+$ cells. Total RNA was extracted to further gene analysis. (*B*) Heatmap showing gene expression correlation between liver CX3CR1$^+$ and F4/80$^+$ cells, splenic dendritic cells (s-DC; CD11c$^+$ F4/80$^-$) and peritoneal macrophages (p-Mϕ). *White dotted square* highlights the genetic proximity between liver CX3CR1$^+$ cells and splenic DCs (correlation ~1). (*C*) Principal coordinates analysis (PCoA) of different isolated cells showing how extravascular CX3CR1$^+$ cells genetically correlate with splenic DCs. (*D*) Functional category analysis based on the gene expression ratio between liver CX3CR1$^+$ and F4/80$^+$ cells evidencing their putative different functions within the liver. (*E*) Same as (*D*), but grouped as functional pathways based on gene ontology. (*F*) Statistically different genes ranked as expression ration of CX3CR1$^+$/F4/80$^+$. n = 3/group.

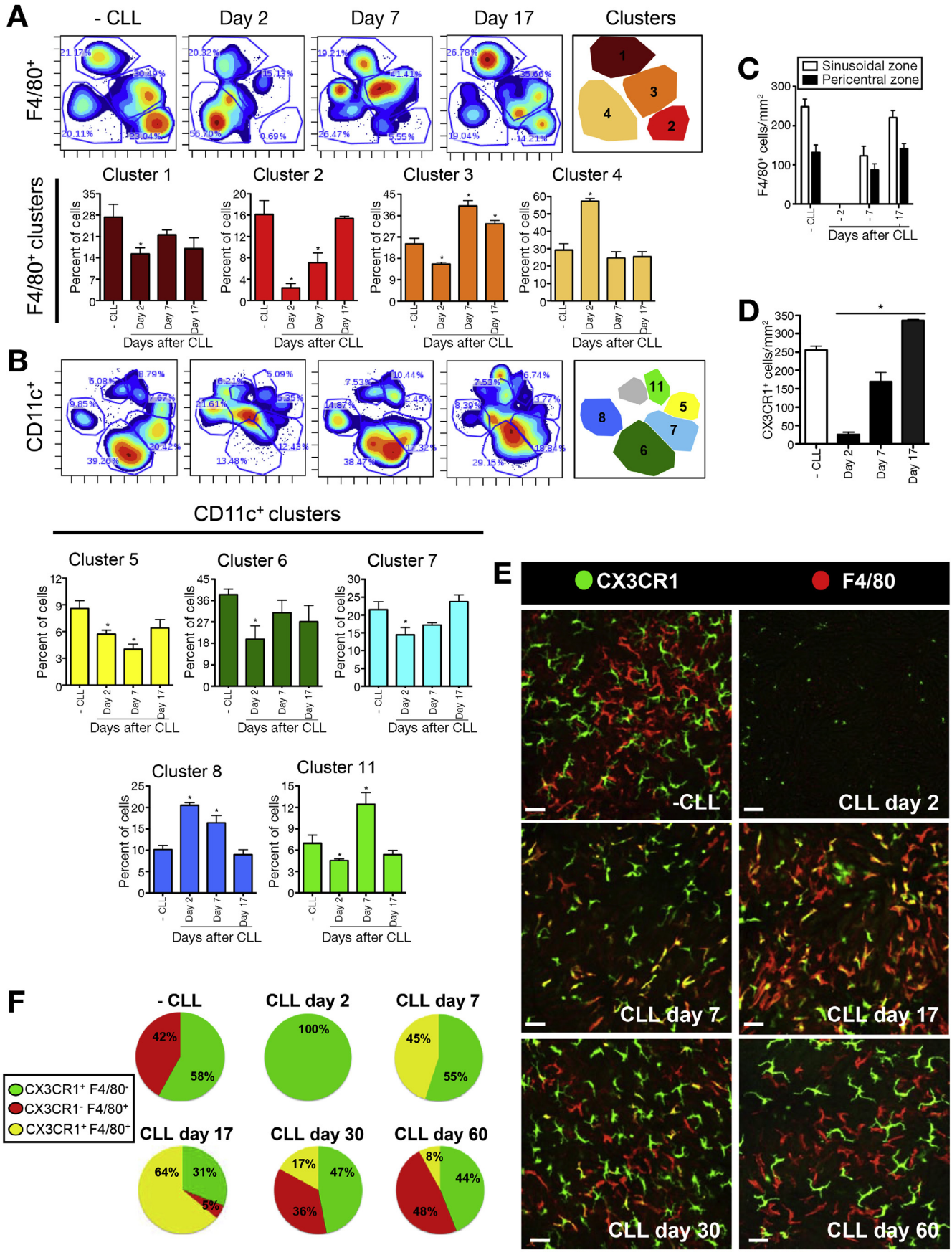
A
- CLL
Day 2
Day 7
Day 17
Clusters
F4/80+
F4/80+ clusters
Cluster 1
Cluster 2
Cluster 3
Cluster 4
Percent of cells
Days after CLL
B
CD11c+
CD11c+ clusters
Cluster 5
Cluster 6
Cluster 7
Cluster 8
Cluster 11
C
Sinusoidal zone
Pericentral zone
F4/80+ cells/mm2
D
CX3CR1+ cells/mm2
E
CX3CR1
F4/80
-CLL
CLL day 2
CLL day 7
CLL day 17
CLL day 30
CLL day 60
F
CX3CR1+ F4/80-
CX3CR1- F4/80+
CX3CR1+ F4/80+
42%
58%
100%
45%
55%
64%
31%
5%
17%
47%
36%
8%
44%
48%

Emergency Repopulation Dynamics After Sudden Phagocyte Depletion

To better understand how these 2 populations are maintained within the liver, we removed liver phagocytes with clodronate-loaded liposomes (CLL), a commonly used method to deplete tissue macrophages, and monitored their replenishment dynamics. Focusing on F4/80-gated clusters (Figure 3*A*), CyTOF analysis showed that the majority of KCs (clusters 2–3) were depleted 2 days after CLL treatment (Figure 3*A* and Supplementary Figure 1*C*). The frequency of infiltrating monocytes was increased (cluster 4), suggesting that these cells may consist in a source of monocyte-derived macrophages. Gating on $CD11c^+$ events (Figure 3*B*), we observed that DC clusters (6, 7, and 11) were also reduced, demonstrating that CLL treatment depletes not only KCs, but also DCs (Figure 3*B*). Intravital imaging confirmed full depletion of KCs (Figure 3*C*) and approximately 95% reduction in DC numbers (Figure 3*D*) after CLL. Of note, the remaining DCs after CLL treatment were mainly the plasmacytoid DCs (cluster 8), which were not affected by CLL (Figure 3*B*). At this time point, $F4/80^+Ly6C^+$ infiltrating monocytes belonging to cluster 4 were highly increased (20.11% in nondepleted group to 56.70% in CLL day 2 group; Figure 3*A*).

One week after depletion, CLL-depleted clusters began to replenish the liver (Figure 3*A* and *B* and Supplementary Figure 6*A*) and infiltrating monocytes (cluster 4) returned to baseline frequency. In vivo imaging showed that the majority of the 2 populations of replenished cells were $CX3CR1^+$ and inhabited the intravascular compartment at the 7^{th} day post depletion (Figure 3*E*). These cells were homogeneously distributed throughout the liver (Figure 3*E*) and F4/80 expression was now (but not at day 2) detected on half of the population of $CX3CR1^+$ cells (Figure 3*F*). Seventeen days after CLL treatment, normal frequencies and numbers of both KC and DC clusters were observed as determined by CyTOF analysis (Figure 3*A* and *B* and Supplementary Figure 6*B*). Almost all cells remained $CX3CR1^+$, whereas F4/80 expression was found on 64% of these cells and a small population of $F4/80^+$ cells (5%) has lost their CX3CR1 expression (Figure 3*E* and *F*). By day 30, 36% of cells were $F4/80^+CX3CR1^-$, with only 17% double-positive cells. After 60 days, cells returned to near baseline distribution, with only 8% remaining $F4/80^+CX3CR1^+$ (Figure 3*F*). Noteworthy is that at day 7, all of the $CX3CR1^+$ cells (half F4/80-positive half negative) were still inside the vasculature, suggesting that their early differentiation occurs in the sinusoids. KC distribution recovered 80% of the baseline values at day 17 after depletion (Figure 4*A* and *B*), while the DC density was still reduced at the same time point, suggesting that DCs have slower repopulation kinetics in comparison with KCs. Normal cell numbers were observed at day 30 for both cell types (Figure 4*A* and *B*). Normalized absolute event numbers corroborated frequency data from all CyTOF experiments (Supplementary Table 2).

A CXC3CL1 Gradient Drives Extravascular Dendritic Cell Re-establishment

Because CX3CR1 expression was prevalent early in the repopulation period, we hypothesized that a gradient of its ligand, CX3CL1, would guide $CX3CR1^+$ phagocyte precursors initially to the sinusoids and facilitated their differentiation into mature KCs and DCs. In vivo staining revealed that CX3CL1 was constitutively found in the liver microvasculature (Figure 5*A* and *B*) and its expression was increased after depletion and during the first time points of the replenishment phase (2^{nd} and 7^{th} day after CLL; Figure 5*A* and *B*). CX3CL1 was also increased in the extravascular compartment (*arrowheads* on Figure 5*A*) and, after 17 days post-CLL treatment, baseline expression of CX3CL1 was re-established (Figure 5*A*). This suggests that CX3CL1 production precedes DC extravasation to extravascular spaces. To confirm the role of CX3CL1 on both cell recruitment and distribution, we used $CX3CR1^{gfp/gfp}$ (deficient) mice and found approximately 50% less liver DCs under basal conditions in comparison with the heterozygote strain ($CX3CR1^{gfp/wt}$; Figure 5*C* and *D*). This 50% relative reduction in DC density in CX3CR1-deficient mouse was seen throughout the emergency repopulation period (Figure 5*D*). Interestingly, CX3CR1-deficient mice had about 20%−30% more KCs under basal conditions (Figure 5*E* and *F*), and this small density increase was observed throughout the experimental time (Figure 5*F*). This suggests that CX3CR1 was not required for progenitor cell recruitment and KC development, but was crucial for DC extravasation and survival in the extravascular space. Because CCL2/CCR2 interaction mediates monocyte egress from BM and their further recruitment into tissues, we also investigated the contribution of CCR2 to phagocyte seeding within the liver. In sharp contrast to the absence of CX3CR1, $CCR2^{-/-}$ mice have normal KC/DC distribution and density (Supplementary Figure 5*E* and *F*). In addition, CCR2 seems not to contribute to further DC emigration and maturation within the extravascular compartment.

Figure 3. Emergency repopulation dynamics of liver phagocytes. (*A*) Density *dot plot* from CyTOF showing clustered populations based on F4/80 expression during phagocyte replenishment period and percentage of cells in the different $F4/80^+$ clusters during phagocyte replenishment period. Mice were treated with CLL (200 μL) at day 0, and evaluated in different time points. (*B*) Same as (*A*), but for CD11c expression. (*C*) Quantification of $F4/80^+$ cells in different liver zones showing their heterogeneous distribution and their recovery to normal number and location after 17 days. (*D*) Same as (*C*), but for $CX3CR1^+$ cells ($CX3CR1^{gfp/wt}$ mice). (*E*) Liver intravital microscopy throughout phagocyte repopulating period. (*F*) Quantification of $CX3CR1^+$, $F4/80^+$ or double-positive cells from intravital microscopy. Scale bars = 40 μm. Error bars indicate the mean ± SEM. $^*P < .05$ (unpaired *t* test), in comparison to –CLL group. n = 5/group.

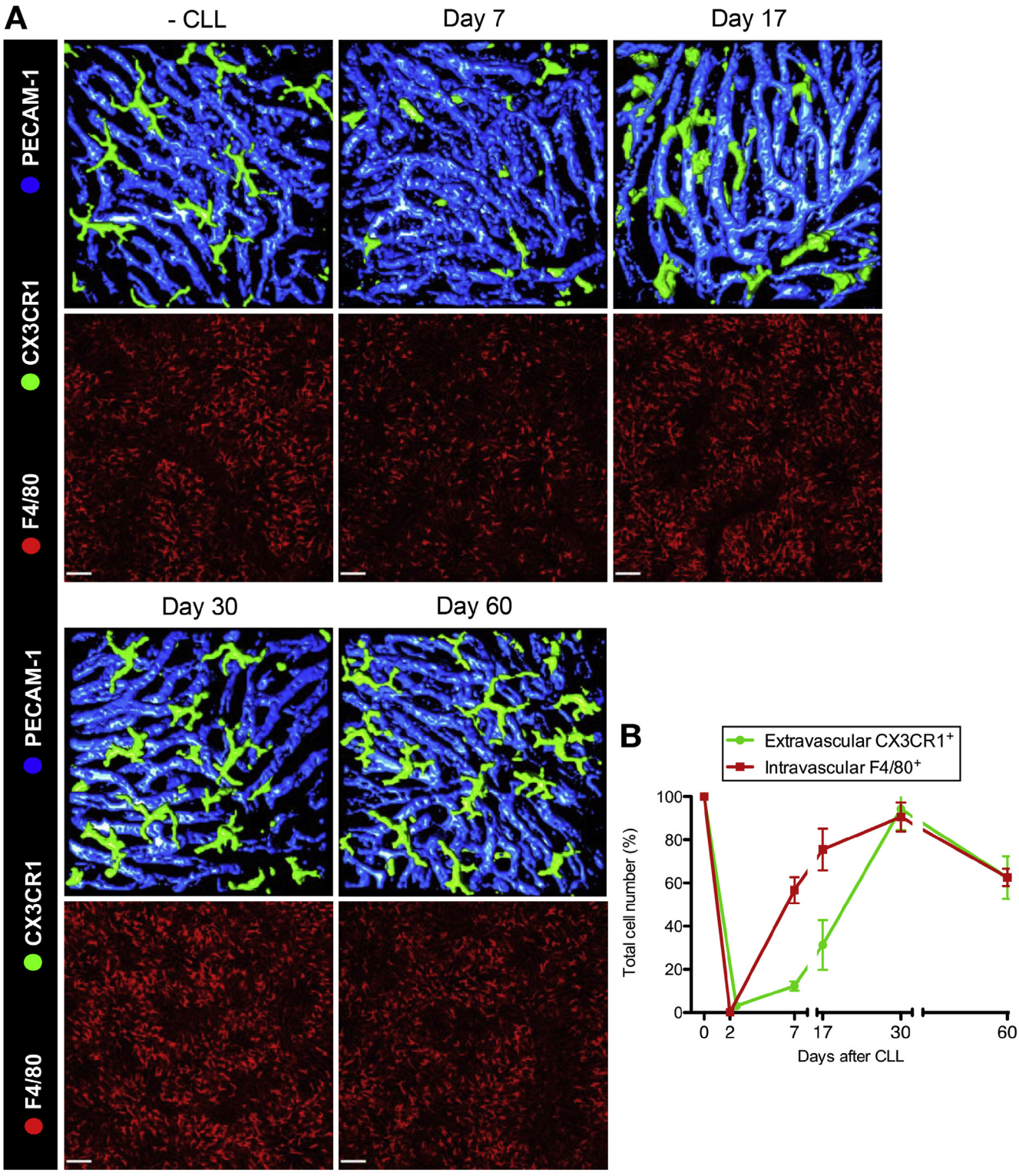

Figure 4. Differential repopulation kinetics of DCs and KCs. (*A*) Liver intravital microscopy images from different time points after clodronate injection. *Upper panel* shows extravascular CX3CR1^{+} cells (in *green*, 3-dimensional rendering; CX3CR1$^{gfp/wt}$ mice). Sinusoids were evidenced in *blue* (anti–PECAM-1 antibody). KCs (intravascular F4/80^{+} cells stained with anti-F4/80 antibody) are depicted in *lower panels*. (*B*) Quantification of cell numbers over the repopulation period in comparison to baseline values (adjusted to 100% as control). *Scale bars* = 120 μm.

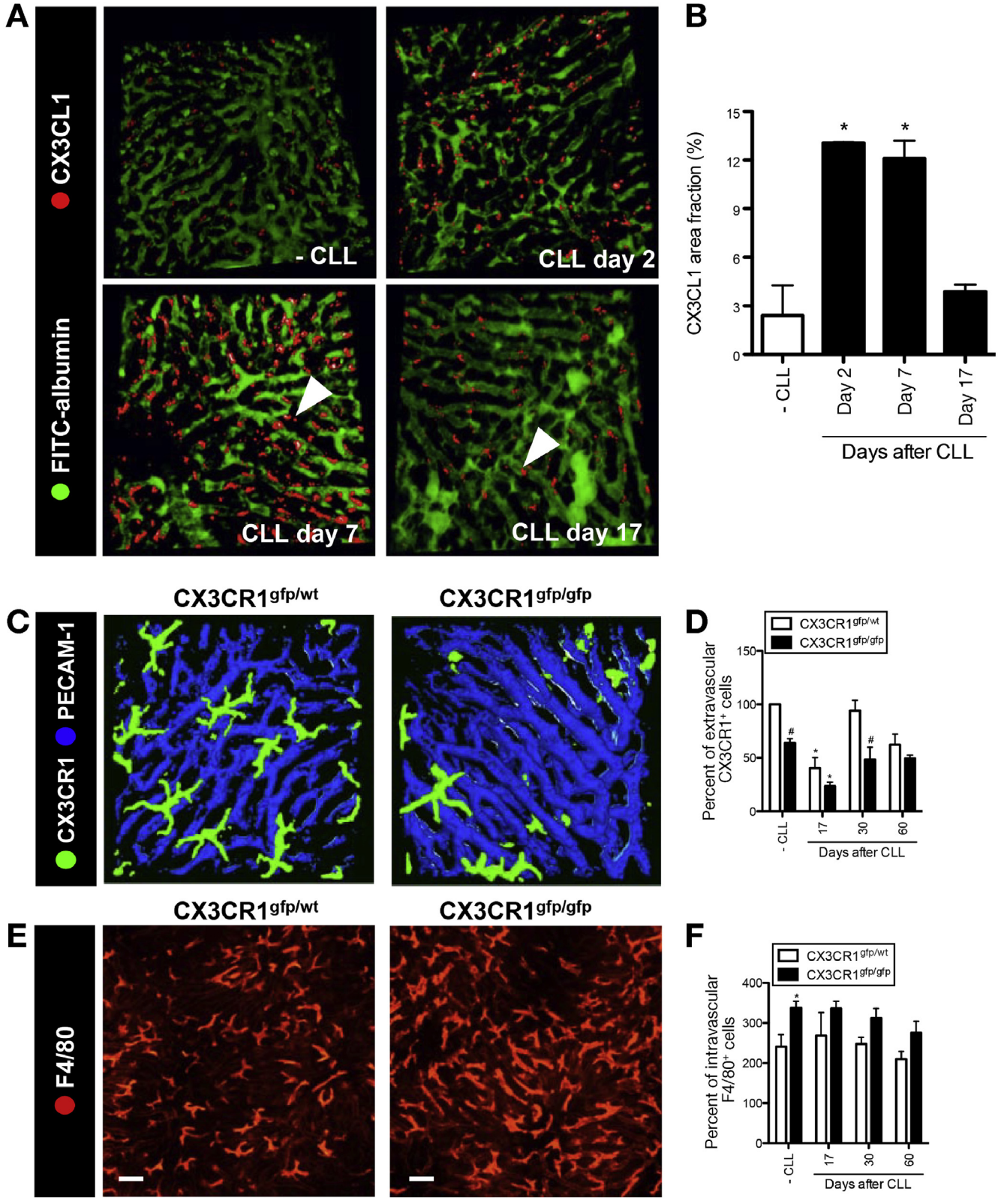

Figure 5. CX3CR1 guides BM precursors to repopulate the liver. (*A*) Liver intravital microscopy showing the expression and distribution of CX3CL1 (in *red*; anti-CX3CL1) and (*B*) digital quantification of CX3CL1 distribution within the liver. Vessels were stained by intravenous injection of fluorescein isothiocyanate albumin (5 mg/kg). (*C*) Liver intravital microscopy from $CX3CR1^{gfp/wt}$ and $CX3CR1^{gfp/gfp}$ (deficient) mice showing the reduced number of extravascular DCs in deficient mice. (*D*) Quantification of extravascular $CX3CR1^{+}$ cells during repopulation period. (*E*) Same as (*C*), but for intravascular $F4/80^{+}$ cells. (*F*) Same as (*D*), but for intravascular $F4/80^{+}$ cells. Scale bars = 40 μm. $^{*}P < .05$, in comparison with vehicle-treated group and $^{\#}P < .05$ in comparison to –CLL group of the respective time point (one-way analysis of variance test). n = 5/group.

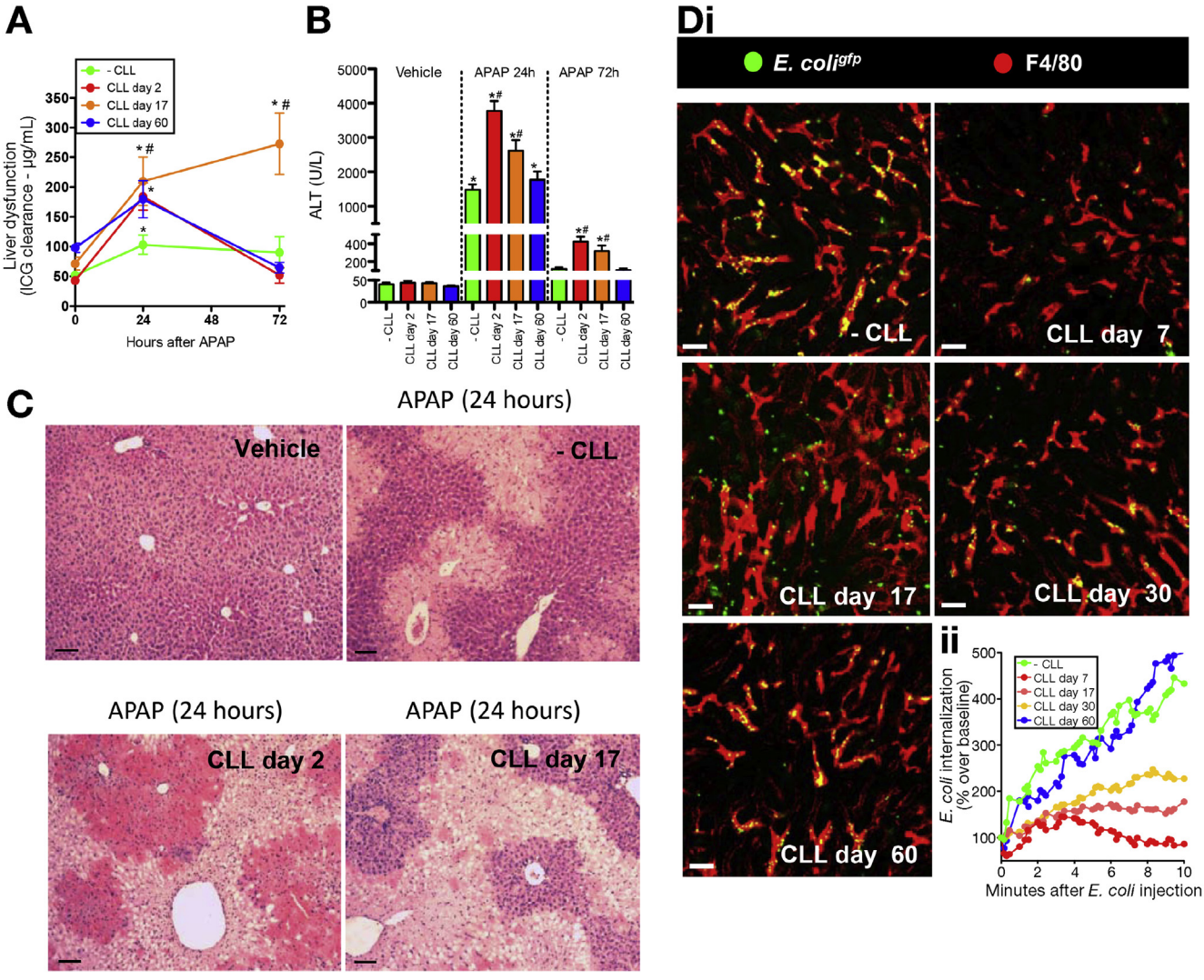
A
- CLL
CLL day 2
CLL day 17
CLL day 60
Liver dysfunction (ICG clearance - µg/mL)
Hours after APAP
B
Vehicle
APAP 24h
APAP 72h
ALT (U/L)
C
APAP (24 hours)
Vehicle
- CLL
CLL day 2
CLL day 17
Di
E. coli gfp
F4/80
- CLL
CLL day 7
CLL day 17
CLL day 30
CLL day 60
ii
E. coli internalization (% over baseline)
Minutes after E. coli injection

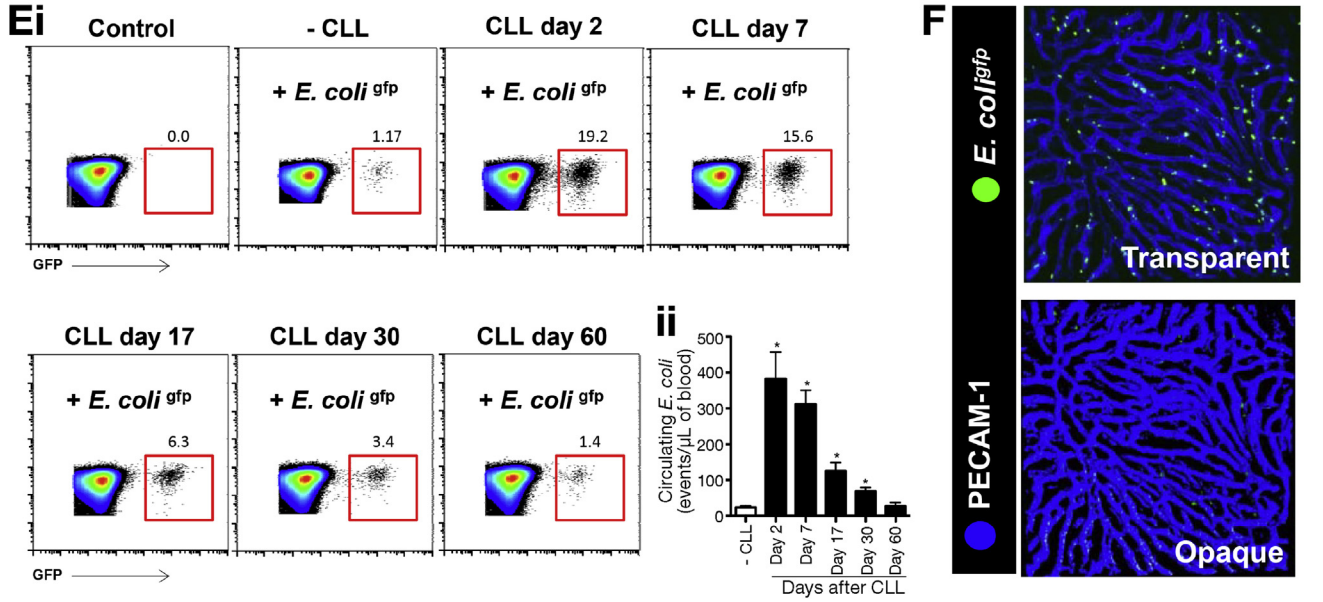
Ei
Control
- CLL
CLL day 2
CLL day 7
CLL day 17
CLL day 30
CLL day 60
+ E. coli gfp
0.0
1.17
19.2
15.6
6.3
3.4
1.4
GFP
ii
Circulating E. coli (events/µL of blood)
Days after CLL
F
E. coli gfp
PECAM-1
Transparent
Opaque

To test whether the BM is the major source of intravascular precursors that replenish the liver, we transplanted GFP-expressing BM precursors to gamma ray–irradiated mice. Intravital imaging confirmed that approximately 99% of liver KCs and also extravascular DCs were derived from the BM (Supplementary Figure 7*A*). Altogether, we demonstrated that both KC and DC replenishment occurs initially via myeloid precursors that accumulate within the sinusoids after depletion. Cells that sustain CX3CR1 expression emigrate toward the extravascular compartment by following a CX3CL1 gradient, thus re-establishing the DC population.

Phagocyte depletion and replenishment imprints a temporary altered response to injury

Acute liver failure is a worldwide medical concern, and it is becoming increasingly clear that liver immune cells play a key role in the pathogenesis. In these situations, the local milieu of immune cells is thought to be set toward a regulatory phenotype that minimizes liver injury after toxicity and other pathogenic events. Thus, we investigated the impact of the absence of hepatic phagocytes in a model of APAP-induced sterile liver injury. To better define the clinical impact of our procedures, we directly assessed liver metabolic function by monitoring the hepatic clearance rate of ICG, an excellent index of liver function. Phagocyte depletion by CLL led to overt liver dysfunction after APAP administration in comparison with nondepleted mice (Figure 6*A*). In addition, absence of phagocytes delayed recovery to normal function after APAP challenge (Figure 6*A*). Of note, APAP administration alone also caused significant reduction in KC numbers (approximately 40% reduction; Supplementary Figure 7*B*).

To explore the consequences of replacement of native phagocytes by BM-derived cells, we challenged mice with APAP at different stages after replenishment. After 17 days of CLL-induced depletion, APAP-treated mice still had worse liver dysfunction in comparison with the nondepleted group (Figure 6*A*). In addition, although liver metabolic function was completely restored in nondepleted mice after 3 days of APAP overdose, replenished mice had delayed return of liver function after 17 days of CLL treatment (Figure 6*A*). Serum transaminase quantification (alanine aminotransferase) and histopathology during APAP-mediated liver injury and recovery confirmed the metabolic function assessed by our ICG clearance protocol (Figure 6*B* and *C*). Interestingly, this increased injury was not observed at the earliest time (2 days) after CLL depletion, suggesting that the cells must first fully seed the liver, at which point they harbor a pro-inflammatory phenotype until at least 17 days. Nevertheless, liver response to injury was completely restored after 60 days of replenishment (Figure 6*A* and *B*), demonstrating that despite a transient hyperresponsiveness profile during the initial phases of replenishment, the liver recovers its normal regenerative ability. In line with this, normal KC distribution was also observed 17 to 30 days after APAP-induced acute hepatitis (Supplementary Figure 7*B*).

Phagocytic Instruction of Bone Marrow–Derived Kupffer Cells During Replenishment

To investigate whether BM-derived phagocytes functioned in the same fashion as yolk sac–derived cells during infection, we assessed phagocytic function at different stages of replenishment after clodronate depletion. For this, GFP-expressing *E coli* were injected intravenously and bacterial capture was evaluated in real time using intravital microscopy (Figure 6*Di* and *Dii*). High-magnification imaging revealed that free-flowing *E coli* were immediately immobilized to the KC membrane at first contact, and no pseudopod formation or major changes in KC morphology seemed to be necessary for initial bacterial arrest (Supplementary Movies 5 and 6). This highlights that the mechanisms involved in rapid bacterial clearance exerted by KCs under shear may be different from other classic phagocytosis processes. Imaging experiments were complemented by flow cytometry quantification of free bacteria in the blood (Figure 6*Ei*). Naïve mice efficiently cleared *E coli* from circulation (Figure 6*Ei* and *Eii*); however, increased numbers of circulating *E coli* were observed in mice that were either depleted (CLL 2 days; Supplementary Movie 6) or fully replenished (up to 17 days after CLL; Figure 6*F* and *G* and Supplementary Movie 6). In fact, intravital imaging showed that KC adhesiveness to *E coli* was dramatically reduced in immature KCs, and despite brief bacterial interactions with KC membrane, only a few bacteria were arrested and internalized (Figure 6*Di* and *Dii*, Supplementary Movies 5 and 6). Therefore, despite normal cell density and location, newly arrived KCs have reduced phagocytic capacity for at least 17 days. In agreement,

Figure 6. Substitution of phagocytes imprints a temporary altered response to injury and infection. Assessment of liver function (*A*) and (*B*) injury during different times of repopulation period. Mice received a single dose of ICG (20 mg/kg) and its clearance from the circulation was measured over the time. (*C*) Liver histopathology analysis from mice treated with APAP (500 mg/kg) after different periods of repopulation confirming overt injury in repopulated mice. (*Di*) In vivo imaging of *E coli*^{gfp} capture by KCs (F4/80^{+}) in control mice and at different time points after phagocyte depletion. (*Dii*) Digital quantification of *E coli*^{gfp} accumulation inside KCs expressed as increased over the baseline (set as 100% as the first frame after injection. (*Ei*) Quantification of free-flowing *E coli*^{gfp} by fluorescence-activated cell sorting (FACS) in the blood during repopulation period. *Numbers* in the gates are GFP^{+} events/μL. (*Eii*) Serum *E coli*^{gfp} concentration normalized by blood volume. Data collected from FACS. (*F*) Liver intravital microscopy evidencing the exclusive intravascular location of GFP-expressing *E coli*. *Scale bars* in (*C*) = 100 μm, and in (*Di* and *E*) = 65 μm. Error bars indicate the mean ± SEM. $^{*}P < .05$, in comparison with vehicle-treated group and $^{\#}P < .05$ in comparison to –CLL group of the respective time point (one-way analysis of variance test). n = 5/group.

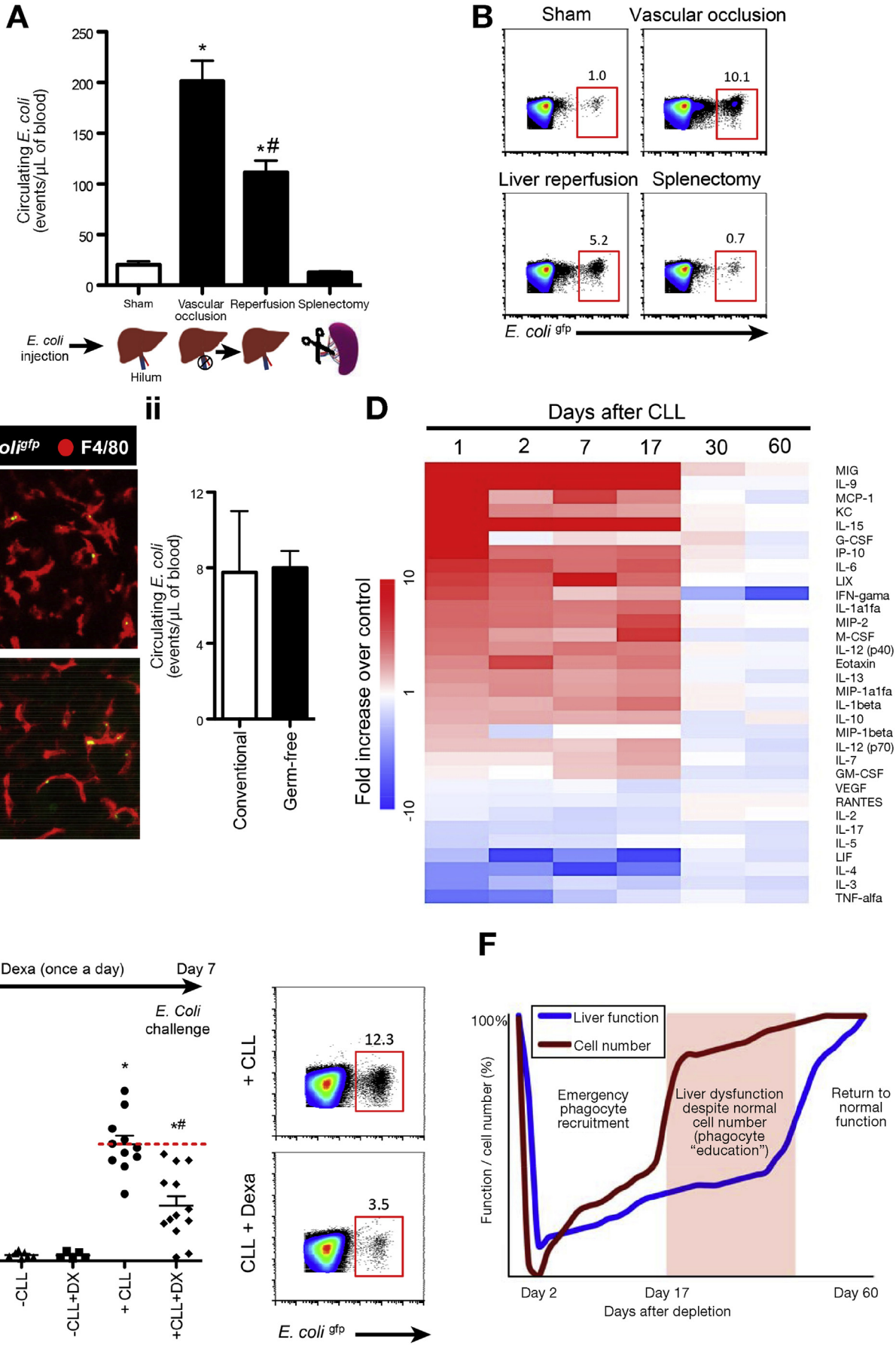
A
Circulating E. coli (events/µL of blood)
250
200
150
100
50
0
*
*#
Sham
Vascular occlusion
Reperfusion
Splenectomy
E. coli injection
Hilum
B
Sham
Vascular occlusion
1.0
10.1
Liver reperfusion
Splenectomy
5.2
0.7
E. coli gfp
Ci
E. coli gfp
F4/80
Conventional
Germ-free
ii
Circulating E. coli (events/µL of blood)
12
8
4
0
Conventional
Germ-free
D
Days after CLL
1
2
7
17
30
60
Fold increase over control
10
1
-10
MIG
IL-9
MCP-1
KC
IL-15
G-CSF
IP-10
IL-6
LIX
IFN-gama
IL-1a1fa
MIP-2
M-CSF
IL-12 (p40)
Eotaxin
IL-13
MIP-1a1fa
IL-1beta
IL-10
MIP-1beta
IL-12 (p70)
IL-7
GM-CSF
VEGF
RANTES
IL-2
IL-17
IL-5
LIF
IL-4
IL-3
TNF-alfa
E
Day 1
Dexa (once a day)
Day 7
CLL
E. Coli challenge
Circulating E. coli (events/µL of blood)
300
200
100
0
*
*#
-CLL
-CLL+DX
+ CLL
+CLL+DX
+ CLL
12.3
CLL + Dexa
3.5
E. coli gfp
F
100%
Liver function
Cell number
Function / cell number (%)
Emergency phagocyte recruitment
Liver dysfunction despite normal cell number (phagocyte "education")
Return to normal function
Day 2
Day 17
Day 60
Days after depletion

adoptive transfer of BM isolated cells to recently depleted mice caused no detectable improvement in bacterial clearance after at least 1 week, confirming that even when precursors are delivered in high numbers into the circulation, a period of adaptation within the liver microenvironment is required for KC education (data not shown). Between 30 and 60 days of replenishment, normal phagocytic activity and clearance of circulating *E coli* were restored (Figure 6*Ei* and *Eii* and Supplementary Movie 5). Because only a few *E coli* were seen in the extravascular compartment or interacting with DCs, we suggest that KCs are the primary cell population involved in rapid *E coli* capture within the liver (Figure 6*F* and Supplementary Movie 7), while DCs seems to be involved in further antigen presentation, as shown by gene expression assays.

To investigate whether the liver was the main site for systemic *E coli* removal, we interrupted the hepatic blood flow using a transitory vascular occlusion approach. In fact, higher numbers of circulating *E coli* were found when the blood was not circulating through the liver, and liver reperfusion significantly restored *E coli* clearance (Figure 7*A* and *B*). Although systemic CLL treatment also depletes splenic resident macrophages that may be involved in bacterial sequestration from the circulation, splenectomized mice had efficient systemic *E coli* clearance throughout the experiment (Figure 7*A* and *B*). Together, these data reveal a window of hepatic phagocytic dysfunction while KC maturation occurs.

A long-term exposure to microbe-associated molecular patterns from the portal tract could be important for maturation of newly recruited precursors. However, in the absence of commensal microbiota (germ-free mice), KCs had a normal ability to clear systemic bacteria (Figure 7*Ci* and *Cii*), despite minor morphologic and numeric differences (data not shown). Therefore, we hypothesized that intrinsic liver-derived factors shaped KC function during replenishment. To explore this, hepatic inflammatory status was evaluated using a multiplexed cytokine approach. After 1 day of CLL treatment, an increase of several proinflammatory cytokines was observed in comparison with nondepleted mice (Figure 7*D* and Supplementary Table 3), including interleukin (IL) 6, interferon (IFN) γ, KC/CXCL1, and IL9. Concomitantly, IL3, IL4, and tumor necrosis factor (TNF)$-\alpha$ were down-regulated after depletion (Figure 7*D*). Other cytokines that have been implicated in support and replenishment of stromal and myeloid cells, such as lipopolysaccharide-induced CXC chemokine, were highly expressed and sustained up to 17 days post-depletion (Figure 7*D*), entirely consistent with the observed liver dysfunction. Thus, phagocyte depletion and replenishment imprinted a transitory pro-inflammatory signature in the liver, suggesting that such changes in the liver microenvironment could explain the rapid infiltration of phagocyte precursors and also the altered response to bacterial clearance. To dampen liver inflammation triggered by phagocyte depletion, we chronically treated mice with a broad-spectrum anti-inflammatory drug (dexamethasone) during the first week of the replenishment phase. Intriguingly, dexamethasone-treated mice had a significantly faster recovery of *E coli* extraction from circulation (Figure 7*E*). Nondepleted mice treated with dexamethasone under the same conditions were not different from controls (Figure 7*E*). Consistent with this, the liver responded normally to inflammation and bacterial challenge after 60 days of depletion, which was associated with the return of hepatic inflammatory mediators to baseline levels (Figure 7*E*).

Discussion

Using a previously unreported combination of mass cytometry, confocal intravital microscopy, and multiplexed gene expression array, we precisely described the different immune phenotypes, morphology, density, and location of liver phagocytes. We show that there is a vast population of liver DCs, and part of these cells are located in the subcapsular space and not just between hepatocytes or in the vasculature, as suggested previously.[24] This strategic localization may also allow for inter-compartment communications among the liver parenchyma and sinusoids, the mesothelium, and perhaps even the peritoneal cavity.[25] Considering their repertoire of cell surface receptors and gene expression, this population of liver DCs might also process and present antigens like a number of the other DC subtypes. Despite the different origins of native KCs and DCs, we demonstrated using a high-dimensional immunophenotyping approach that myeloid precursors were able to fully restore normal cell density and location after depletion, and this is likely to occur after their recruitment via an intravascular route. Importantly, liver phagocyte density can also be re-established to normal values, even after a full depletion methodology using clodronate,

Figure 7. Re-establishment of liver function after phagocyte educational period is dependent on hepatic environment rather than bacterial clues. (*A*) Circulating *E coli* number in mice submitted to temporary hepatic vascular occlusion (HVO; 5 minutes), reperfused (5 minutes after reperfusion), and splenectomized mice (1 hour before *E coli* challenge) in comparison to sham-operated group. (*B*) Same as (*A*), but analyzed by fluorescence-activated cell sorting (FACS). Numbers in the gates are GFP^+ events/μL. (*Ci*) Liver intravital microscopy showing similar phagocytic ability of KCs from germ-free and conventional mouse. (*Cii*) Free *E coli* quantification by FACS in the blood of conventional and germ-free mouse. (*D*) Fold increase of different inflammatory mediators after phagocyte depletion and replenishment in comparison with controls assessed by Luminex. Here, controls were set as fold = 1, therefore, have *white color code*. (*E*) Chronic dexamethasone treatment (5 mg/kg, once a day for 7 days) accelerated liver return to normal bacterial clearance, as shown by flow cytometry. (*F*) Graphical abstract showing our main conclusions regarding the different dynamics of phagocyte repopulation and recovery of liver function. *Scale bars* = 65 μm. Error bars indicate the mean (±SEM). Scale bars = 16 μm. $^*P < .05$ (unpaired *t* test) in comparison with sham. $^{\#}P < .05$ (one-way analysis of variance test) in comparison with HVO group. n = 5/group.

showing that self-replication is not entirely necessary to a complete re-establishment of phagocytic populations. Also, myeloid progenitors can replenish both the KC and DC population into 2 different anatomic compartments. In fact, the KC and DC precursors adhered within the sinusoids and 2 phenotypes were observed: some moved no further, while others adhered in the same sinusoids and followed a gradient of the ligand for CX3CR1 to emigrate out of the vasculature. CX3CR1/CX3CL1 interaction was critical to re-establish the liver DC, but not the KC population, but because the majority of the intravascular precursors expressed the receptor for CX3CL1, it raises the question why some of the cells remained in the sinusoids to become KCs, while others emigrated into the extravascular parenchymal space.

Using CyTOF, we identified that under baseline conditions, liver $CD11c^+$ cells are not exclusively DCs as previously assumed,[26] but are rather also a subset of KCs that express this marker. It was recently described that new BM-derived KCs can adopt a genetic profile that may resemble their native counterparts.[27] Here we expanded these findings, showing that intravascular precursors restored KC/DC density and location after full depletion by clodronate or irradiation, but for at least 17–30 days, repopulated livers did not reach their optimal tolerogenic levels and were still more prone to collateral damage. Also, KCs may have a unique mechanism to rapidly arrest bacteria under shear that involves initial "passive" bacterial adhesion to the cell surface, and further internalization. Interestingly, newly emigrated KCs had defective *E coli* catching from the circulation, indicating a further maturation requirement of the KCs and a putative enhanced susceptibility to bacterial spread. It is reasonable to suggest that several molecules involved in phagocytic processes that are expressed by KCs under normal conditions may be reduced in immature KCs, and may reach optimal expression levels during the maturation process. Because KCs from germ-free mice had fully functional systemic bacterial catching, it is likely that the phagocytic ability—and perhaps also their dysfunction—are not dependent on instructions from microbiota, but probably from endogenous mediators that compose the hepatic environment.[28]

Although we initially thought that inflammatory mediators might induce the necessary receptors for bacterial catching and tolerance in the maturing KC, the opposite was true. When we dampened liver inflammatory response, proper phagocytosis by KCs was reached at earlier time points. This suggests that therapeutic interventions aimed to block overt inflammation might also help patients that suffered from extensive liver injury or were subjected to irradiation, conditions where a substantial part of liver phagocytes might have been depleted. After 60 days replenishment time, the liver responded normally to injury, and reacquired efficient bacterial clearance function. This implies that despite the normal number and distribution of phagocytes at earlier time points after replenishment, an "educational period" is required for the restitution of normal function of these cells. Thus, it is possible that the liver has a unique secretome signature that maintains tissue-resident populations and that education of precursors requires up to 30–60 days for full maturation. Collectively, these findings provide insight into the mechanisms involved in relatively higher susceptibility to collateral liver injury and systemic infection observed during extensive liver damage and also in patients that were subjected to full body irradiation.

Supplementary Material

Note: To access the supplementary material accompanying this article, visit the online version of *Gastroenterology* at www.gastrojournal.org, and at http://dx.doi.org/10.1053/j.gastro.2016.08.024.

References

1. Epelman S, Lavine KJ, Randolph GJ. Origin and functions of tissue macrophages. Immunity 2014;41:21–35.
2. Ginhoux F, Jung S. Monocytes and macrophages: developmental pathways and tissue homeostasis. Nat Rev Immunol 2014;14:392–404.
3. Wisse E, van't Noordende JM, van der Meulen J, et al. The pit cell: description of a new type of cell occurring in rat liver sinusoids and peripheral blood. Cell Tissue Res 1976;173:423–435.
4. Bendelac A, Savage PB, Teyton L. The biology of NKT cells. Annu Rev Immunol 2007;25:297–336.
5. Thomson AW, O'Connell PJ, Steptoe RJ, et al. Immunobiology of liver dendritic cells. Immunol Cell Biol 2002;80:65–73.
6. Jenne CN, Kubes P. Immune surveillance by the liver. Nat Immunol 2013;14:996–1006.
7. Lee SJ, Park SY, Jung MY, et al. Mechanism for phosphatidylserine-dependent erythrophagocytosis in mouse liver. Blood 2011;117:5215–5223.
8. Terpstra V, van Berkel TJ. Scavenger receptors on liver Kupffer cells mediate the in vivo uptake of oxidatively damaged red blood cells in mice. Blood 2000;95:2157–2163.
9. Balmer ML, Slack E, de Gottardi A, et al. The liver may act as a firewall mediating mutualism between the host and its gut commensal microbiota. Sci Transl Med 2014;6:237ra66.
10. Wong CH, Jenne CN, Petri B, et al. Nucleation of platelets with blood-borne pathogens on Kupffer cells precedes other innate immunity and contributes to bacterial clearance. Nat Immunol 2013;14:785–792.
11. Yona S, Kim KW, Wolf Y, et al. Fate mapping reveals origins and dynamics of monocytes and tissue macrophages under homeostasis. Immunity 2013;38:79–91.
12. Schulz C, Gomez Perdiguero E, Chorro L, et al. A lineage of myeloid cells independent of Myb and hematopoietic stem cells. Science 2012;336:86–90.
13. Liu K, Nussenzweig MC. Origin and development of dendritic cells. Immunol Rev 2010;234:45–54.
14. Matsuno K, Ezaki T, Kudo S, et al. A life stage of particle-laden rat dendritic cells in vivo: their terminal division,

active phagocytosis, and translocation from the liver to the draining lymph. J Exp Med 1996;183:1865–1878.
15. Sato T, Yamamoto H, Sasaki C, et al. Maturation of rat dendritic cells during intrahepatic translocation evaluated using monoclonal antibodies and electron microscopy. Cell Tissue Res 1998;294:503–514.
16. Woo J, Lu L, Rao AS, et al. Isolation, phenotype, and allostimulatory activity of mouse liver dendritic cells. Transplantation 1994;58:484–491.
17. Waite JC, Leiner I, Lauer P, et al. Dynamic imaging of the effector immune response to listeria infection in vivo. PLoS Pathog 2011;7:e1001326.
18. Marques PE, Antunes MM, David BA, et al. Imaging liver biology in vivo using conventional confocal microscopy. Nat Protoc 2015;10:258–268.
19. Lee WY, Moriarty TJ, Wong CH, et al. An intravascular immune response to Borrelia burgdorferi involves Kupffer cells and iNKT cells. Nat Immunol 2010;11:295–302.
20. Becher B, Schlitzer A, Chen J, et al. High-dimensional analysis of the murine myeloid cell system. Nat Immunol 2014;15:1181–1189.
21. Marques PE, Oliveira AG, Pereira RV, et al. Hepatic DNA deposition drives drug-induced liver injury and inflammation in mice. Hepatology 2015;61:348–360.
22. McDonald B, Pittman K, Menezes GB, et al. Intravascular danger signals guide neutrophils to sites of sterile inflammation. Science 2010;330:362–366.
23. Ginhoux F, Liu K, Helft J, et al. The origin and development of nonlymphoid tissue CD103+ DCs. J Exp Med 2009;206:3115–3130.
24. Heymann F, Tacke F. Immunology in the liver—from homeostasis to disease. Nat Rev Gastroenterol Hepatol 2016;13:88–110.
25. Wang J, Kubes P. A reservoir of mature cavity macrophages that can rapidly invade visceral organs to affect tissue repair. Cell 2016;165:668–678.
26. Connolly MK, Ayo D, Malhotra A, et al. Dendritic cell depletion exacerbates acetaminophen hepatotoxicity. Hepatology 2011;54:959–968.
27. Scott CL, Zheng F, De Baetselier P, et al. Bone marrow-derived monocytes give rise to self-renewing and fully differentiated Kupffer cells. Nat Commun 2016;7:10321.
28. Corbitt N, Kimura S, Isse K, et al. Gut bacteria drive Kupffer cell expansion via MAMP-mediated ICAM-1induction on sinusoidal endothelium and influence preservation-reperfusion injury after orthotopic liver transplantation. Am J Pathol 2013;182:180–191.

Received July 14, 2016. Accepted August 21, 2016.

Reprint requests
Address requests for reprints to: Gustavo Batista Menezes, PhD, Center for Gastrointestinal Biology, ICB Room N3-140, Federal University of Minas, Belo Horizonte, Minas Gerais, 31270-901, Brazil. e-mail: menezesgb@ufmg.br; fax: +55 31 3409 2770; or Paul Kubes, PhD, Calvin, Phoebe and Joan Snyder Institute for Chronic Diseases, Department of Physiology and Pharmacology, Cumming School of Medicine, University of Calgary, Alberta, T2N 4N1, Canada. e-mail: pkubes@ucalgary.ca; fax: (403) 270–7516.

Acknowledgments
The authors thank Dr Julio Scharfstein and Dr Clarissa Nascimento for providing CD11c-EYFP mice (UFRJ, Brazil) and Dr Howard Weiner, Dr Shirong Liu (Harvard Medical School, Boston, MA), Giuliana Bertozi (FMRP, Universidade de São Paulo, Brazil), and Dr Flaviano Martins (UFMG, Brazil) for assistance, reagents, and mice strains. We thank Rodrigo Nogueira, Paulo Lutero de Mello e Silva II, and Dr Denise Cara for helping in the generation of scientific divulgation material. Also, we would like to thank the Centro de Aquisição e Processamento de Imagens (CAPI- ICB/UFMG) and the Flow Cytometry facility of Centro de Pesquisas René Rachou (FIOCRUZ-MG).
GEO accession number: GSE81645.

Conflicts of interest
The authors disclose no conflicts.

Funding
This work was supported by FAPESP, FAPEMIG, CAPES (Biocomputacional), and CNPq (Brazil), and Canadian Institutes of Health Research and the Heart and Stroke Foundation of Canada.